DESIGN AND MANUFACTURING OF COMPOSITE CHIRAL STRUCTURES WITH MORPHING CAPABILITIES

P. Bettini*, A. Airoldi*, L. Di Landro*, G. Sala* A. Spadoni, M. Ruzzene****
***Dipartimento di Ingegneria Aerospaziale, Politecnico di Milano, Milano - ITALY**
****School of Aerospace Engineering, Georgia Institute of Technology, Atlanta GA - USA**

Keywords: *chiral truss-core airfoil, morphing, composite materials, manufacturing*

Abstract

The paper investigates the response of complex cellular structures made of composite materials that can be exploited for morphing purpose and presents a technique for the manufacturing of such type of structures. The configuration under investigation consists of a chiral truss-core airfoil, whose chord-wise compliance can be exploited for morphing purposes. Numerical results are presented to demonstrate the morphing performance of a composite chiral core airfoil, and to motivate the set up of an efficient manufacturing process.

The developed manufacturing approach allows the assembly of complex structural configurations by bonding of composite elements. The manufactured chiral cells have been tested to prove their capability to undergo large displacement without experiencing failure and detailed numerical model are assessed to predict the non-linear response and the strength of such type of structures.

1 Introduction

In the aerospace field, the typical objective of a morphing concept is to provide airfoils with continuous deformations, and to eliminate the need for flap-type mechanisms [1]. In this sense, a variety of solutions have been proposed to provide aircraft wings and helicopter rotor blades with adaptive capabilities [2,3].

This paper presents the morphing properties of an innovative airfoil design, whose core features a chiral structural network. This particular topology can be designed to allow significant de-cambering deformations, which are obtained with the constitutive material remaining in the elastic range [4]. Such capabilities have been demonstrated first numerically in [5], and subsequently in [4] through a set of experiments performed on an airfoil prototype made of aluminum. The material selection in [4,5] was mostly driven by manufacturing considerations, in full awareness that metallic construction was neither practical nor optimal for the application at hand. The preliminary studies in [4,5] however show the potentials of the chiral airfoil, and motivate the need for an effective manufacturing process which allows the use of composite materials. Composite materials could be better suited to develop feasible technological process. Moreover, their adoption presents several potential advantages. Composites may work at higher strain levels without experiencing permanent deformations or failures with respect to most of metal materials. Very thin laminates having different lay-up sequences and hybrid solutions using different types of fibre reinforcement could be manufactured to tune the stiffness and the strength of the morphing structure. Finally, composites are very well suited to host sensors and actuators to develop effective smart structures.

The aforementioned considerations lead to numerically investigate the potential response of an airfoil hosting a composite chiral structure. Such investigation, carried out by means of a finite element model of the structure are presented in the first part of the paper. Thereafter the technology for manufacturing composite chiral cells is described and the results of an experimental activity performed on the manufactured structures are presented. The produced cells have been subjected to tensile and compressive loading to evaluate the

displacement and the loads at failures, evidencing the weak points of the structures and evaluating the possible onset of permanent deformations. A particular modeling technique, based on explicit finite element computations [6,7], is then assessed to set up a numerical approach capable to predict the response and the failure of the chiral assemblies produced by means of the developed technological process.

2 Compliance characteristics of a composite chiral airfoil

This section describes the performance of an airfoil (Eppler 420) hosting in the core a truss-type structure according to the configuration shown in Fig. 1. The considered design has been selected on the basis of previous investigations presented in [4, 5].
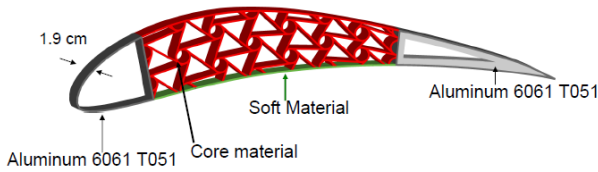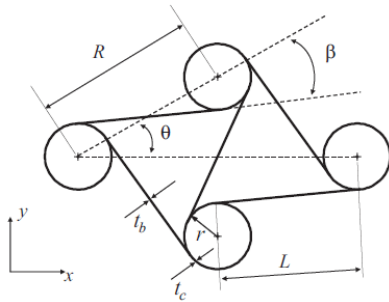

Fig. 1. Chiral core airfoil

Fig. 2. Chiral topology

2.1 Configuration

The chiral network in the airfoil's core is obtained through the assembly of circular elements (nodes), connected by ribs (ligaments) tangent to the nodes. The parameters defining the chiral geometry (see Fig. 2) are R, L, β, t_b, t_c and μ, which in turn represent the distance between the node centers, the rib length, the angle between the imaginary line connecting the circles and a rib, the wall thickness, and the angle defining the ratio of width to height of the

unit cell. These parameters are related as follows: $\tan\beta=2r/L$, $\sin\beta=2r/R$, and $\sin\theta=1/2$.

2.2 Airfoil model

The particular airfoil section is an *Eppler 420* profile. Such highly cambered airfoil is chosen to demonstrate the compliance of the proposed assembly, which constitutes a system with theoretically high-lift at low free-stream velocity, producing de-cambering deformations. As the free-stream velocity is increased the system would tend to a structurally-stable low-camber, low-induced-drag configuration [4, 5].

Based on the findings by the authors in [5], the core layout of the proposed wing concept is obtained through a linear mapping of an initially periodic chiral lattice as described in [4, 5]. For the sake of simplicity and focus on the capabilities of the core arrangement, it is assumed that the leading-edge portion of the truss-core airfoil is clamped, while a concentrated load acts at the upper left corner of the trailing-edge void. Such boundary and loading conditions are identical to the experimental investigations of [4]. Moreover, the core is denoted by an effective topology parameter $L/R \sim 0.90$ after mapping [4, 5].

The objective of the following numerical studies is to estimate the maximum trailing-edge displacement achievable without local failure or yielding. Two possible materials are contemplated, namely: aluminum T6061-051 and a composite laminate made of carbon fabric plies. The onset of the plastic or inelastic responses will be detected carrying out non-linear analyses and modeling the materials by means of a bi-linear constitutive law. The limit of elastic response has been set to the yield stress for the light alloy meanwhile a maximum strain criterion has been chosen for the composite fabric, accepting a maximum strain $\varepsilon_{11max} = 0.01$ in the fiber reinforcement direction either in tension as well as in compression.

The material parameters for each of the investigated materials are reported in Table 1. In order to accurately capture the elastic response of the assembly subject to the aforementioned concentrated load, non-linear analyses also allowed to take into account geometric

stiffening. In particular, a finite-element model, constructed with the commercially available software ANSYS®, including both beam and plane elements is employed. Timoshenko beam elements with finite-strain capabilities (*BEAM23*) are used for the core and outer-profile, while plane elements (*PLANE42*) are assigned to the solid-like trailing-edge section.

The discrepancy in degrees-of-freedom offered by the two element types is circumvented by kinematically constraining rotations of the beam elements to translations of plane element nodes. Each beam-like component of the core is discretized by 24 elements, while the core nodes are discretized by 48 elements. Given that the leading edge is considered clamped a coarser discretization is employed. An implicit Newton-Rapson solution procedure is employed to determine the loading conditions leading to the onset of inelastic response.

Carbon-Fiber CC90 ET443 SEAL	
E_{xx}	56.55 *GPa*
E_{yy}	56.55 *GPa*
ν_{yx}	0.0514
G_{xy}	4.043 *GPa*
σ_{yield}	565.5 *Mpa*
ε_{11max}	0.01

Aluminum T6061-051	
E	68.9 *GPa*
ν_{yx}	0.333
σ_{yield}	276 *Mpa*
ε_{yield}	0.004

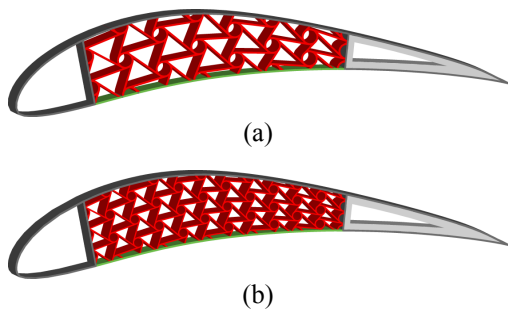Table 1: Elastic constants of considered materials

(a)

(b)

Fig. 3. Considered configurations: (a) 2 cells across airfoil thickness, (b) 3 cells

The influence of core density is also of interest. The three truss-core airfoil configurations depicted in Fig. 3 are considered, whereby the number of accommodated cells across the airfoil thickness is increased in order to obtain smooth and continuous de-camber deformations; the following geometric properties are chosen: node wall thickness t_c = 1.4 *mm* and ligament wall thickness $t_b = 0.8$ *mm*. As discussed in the following sections, the manufacturing process of the experimental chiral core constrained the nodes to be thicker than the ligaments. So the same arrangement is utilized to analyze the performance of the truss-core airfoil.

2.3 Performance

The influence of core material as well as core density on airfoil de-cambering compliance is depicted in Fig. 4. The low core density associated with the 2-cell configuration of Fig. 3-a expectedly yields the highest compliance while the 3-cell configuration yields the highest stiffness.
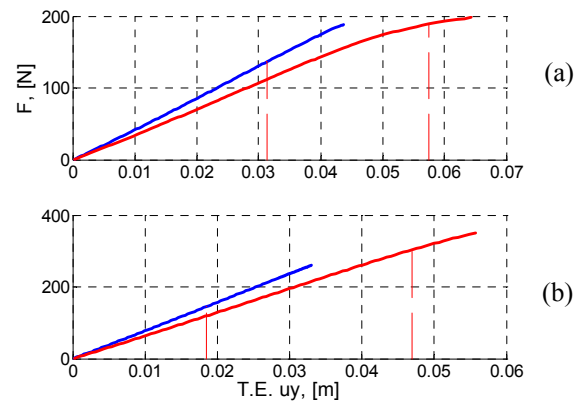

Fig. 4. Airfoil trailing-edge displacement as a function of applied load: 2-cell configuration (a) and 3-cell configuration (b). Blue line, aluminum core, red line carbon-fiber core. Red dashed line, plasticity onset
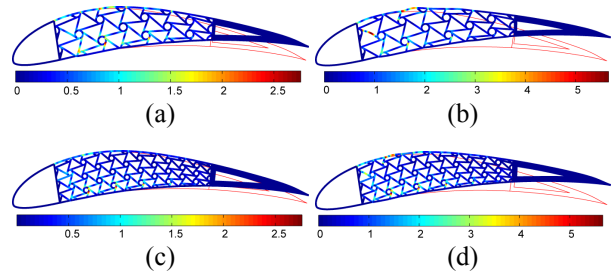

Fig. 5. Axial stress distribution at the onset of plasticity, [*MPa*]. (a) 2-cell aluminum, (c) 3-cell aluminum, (b) 2-cell carbon-fiber, (d) 3-cell carbon fiber

Interestingly, employing carbon fiber as the core material affords a trailing-edge displacement generally twice as large as that obtained with aluminum at the onset of

P. BETTINI*, A. AIROLDI*, L. DI LANDRO*, G. SALA* A. SPADONI**, M. RUZZENE

plasticity. Of note is also the non-linear behavior of the 2-cell configuration with carbon-fiber core (Fig. 4). While the dependency of trailing-edge displacement upon core density and material is intuitive, the stress distribution resulting from the adoption of carbon fiber is not equally so. In particular, the stress distribution for the 2-cell configuration made of aluminum depicted in Fig. 5-a appears confined at the lower portion of the chiral core, while the same configuration with carbon-fiber core features highest axial stress of the ligaments on the upper section of the airfoil profile and ligament closest to the leading edge. As for the findings in [4], the core nodes exhibit much lower stress than the ligaments. The 3-cell configuration also features a significant difference in axial stress in the core for the aluminum and carbon-fiber configuration (Figg. 5-c and 5-d).

3 Manufacturing process

The previous results confirm the potential morphing capability of a composite chiral core applied to an airfoil structure. The set up of a feasible technological process to manufacture such type of structures has been focused on the production of a chiral cell shown in Fig. 6-a. The basic aspects of the developed process are described in the following paragraph. It has been decided to produce ligaments and cylinders by means of classical lamination, by using a vacuum-bag process. Figure 6-b shows the mould prepared to cure the parts of the chiral structure that will be subsequently assembled. The minimum dimension of the elements that can be manufactured in such a way depends on a trade-off between the drapability of the pre-preg material and minimum curvature radii. The assembly of the chiral cells is obtained by a second curing process to bond together the pre-cured parts by means of a structural adhesive film. In the final version of the technology, the separate lamination of cylinders has been eliminated and only ligaments have been produced. The cylinders are obtained by superimposing the curved parts of the ligaments during the assembly (Fig. 6-d). It can be observed that the

strength of the obtained chiral core will strongly depend on the quality of the adhesion between its parts.
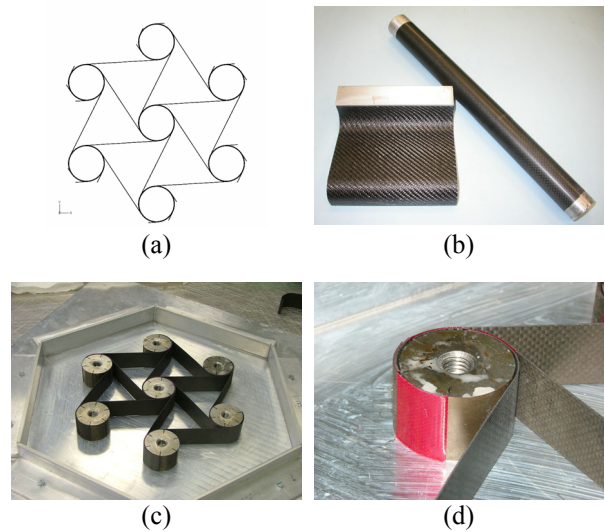

Fig. 6. Manufacturing process: considered chiral cell (a), pre-cured ligaments and cylinders (b), mould assembly (c) and application of adhesive (d)

A specific mould has been conceived for the cell assembly. The hexagonal mould, shown in Fig. 6-c, has a series of metallic cylinders fixed to its lower base to proper position the pre-cured ligaments. The ligaments are positioned introducing the adhesive films between the superimposed curved parts (Fig. 6-d). The assembled mould is then introduced in a vacuum bag and cured in autoclave. The geometrical dimension and the material selection to produce the chiral cell has derived from a trade-off between the evaluated numerical performances and the peculiarities of the technological process. It has been decided to set up the technology avoiding excessively small dimension and curvature radii so to reduce the difficulties in the pre-curing of the ligaments as well as in handling the elements during the final assembly. The L/R ratio of 0.90, already assessed in numerical evaluations, has been chosen and the value of the cylinder radius r has been set to 18 mm. Plain weave fabric plies with a relatively low cured ply thickness of 0.1 mm have been selected to exploit the drapability of fabric without leading to excessively thick laminates. The elastic constants of such fabric materials, evaluated in previous works, are the ones provided in Table 1. Ligaments have been

manufactured using a lay-up sequence of ($[0]_5$), so that 0.5 mm thick laminates have been obtained. AFK-163-2K adhesive film has been used. The overall size of the cells, measured as the distance between the centers of two opposite cylinders turns out to be about 168 mm.

4 Experiments

4.1 Objectives and test set-up

Three cells have been produced by applying the previously described process. Basing on visual inspection, results have been considered acceptable. The strength and the compliance of the cells have then been assessed by means of tests consisting of tensile and compressive cycles performed at very low velocity, that are described in this section.

The experimental activities have been mainly aimed to measure the capability of the cells to undergo large displacement without experiencing permanent deformations, degradation or failures. To accomplish such objective, a simple test lay-out has been adopted. Two opposite cylinders of the cells have been respectively connected the moveable and the fixed cross head of an MTS 858 Static Test System, as shown in Fig. 7-a. The connecting pins have been inserted in rings having the outer diameter matching the inner diameter of the cylinders and allowed to freely rotate about their axis. Each one of the three cells has been subjected to a different loading-unloading cycle, according to the displacement time histories reported in Fig. 7-b.
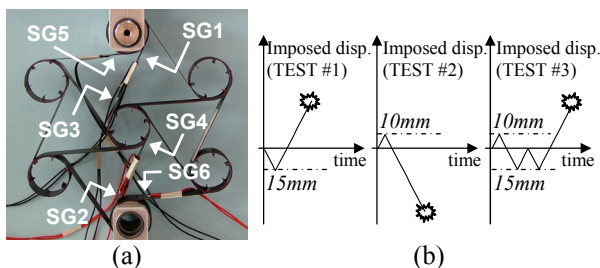
Fig 7 Test lay-out (a) and imposed displacement histories in the three tests (b)

The cross head speed has been to 2 mm/min. The imposed displacement histories allows to detect possible stiffness degradation or permanent deformation occurring after the first loading-unloading cycle.

At the end of tests tensile or compressive failure have been obtained to quantify the cell strength as well as to identify the actual weak points of the assembled structure. Six strain gauges have also been installed on each composite chiral cell, according to the scheme reported in Fig 7-a.

4.2 Result and discussions

Figure 8 reports the force vs. displacement responses obtained in the three performed tests. All the curves shows a non-linear behavior, with a clear tendency to soften in compression and to stiffen in tension. One and three loading-unloading compressive cycles have been carried out in TEST #1 and TEST #3, respectively, before the tensile final loading. The imposed compressive displacement of 15 mm in the preliminary compression cycle corresponds to about 9% of the cell dimension.
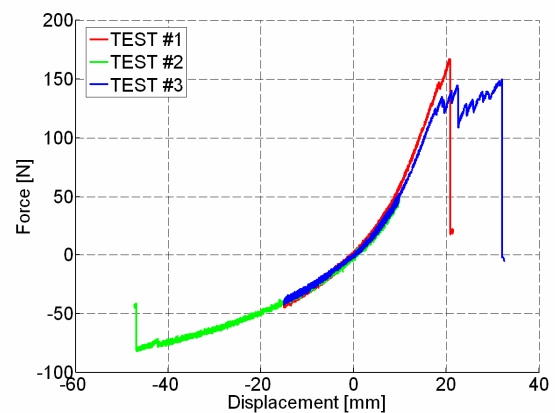

Fig. 8. Force vs displacement responses of the chiral cells

The comparison with the first tensile cycle, performed in TEST #2, shows that the compressive cycles in TEST #1 and TEST #3 have not induced significant permanent deformations as well as stiffness degradation in the cell. Analogously, the tensile loading-unloading cycle, first performed on the cell used in TEST #2, has not induced significant differences in the compressive response with respect to TEST #1 and TEST #3. In such case, the imposed tensile displacement of 10 mm corresponds to about 6% of the cell dimension. Fig. 9 presents a sequence taken from TEST #1.

The compliance of the structure can be appreciated as well as the tendency to transversely contract during the compression and to expand during the tension in accordance with the negative Poisson moduli expected for chiral meta-materials. In TEST #1 final failure occurred in tension for debonding of the ligaments at the upper cylinder in correspondence of a displacement of 20 mm, about 12% of the cell dimension.
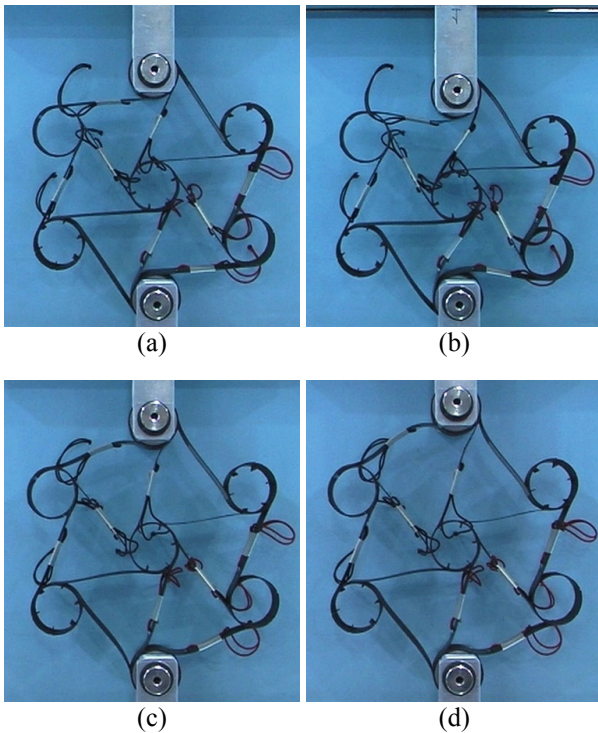

(a)   (b)

(c)   (d)

Fig. 9. TEST #1: initial geometry (a), deformation at maximum compressive displacement (b), deformation during the tensile phase (c), deformation at failure (d)
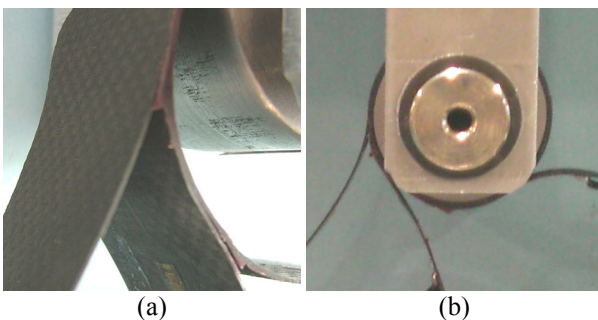

(a)   (b)

Fig. 10. Tensile failure: TEST #1 (a) and TEST #3 (b)

Figure 10-a shows the detail of the failure that occurred with a sudden drop of load carrying capability, although a deviation from the previous regular course can be detected in Fig. 9 at a displacement of 18 mm.

The tensile failure obtained in TEST #3 has been similar: the curve shows a deviation from the regular course at about 18 mm in correspondence of the debonding of the ligaments at the upper as well at the lower cylinder. In TEST #3 however a much more progressive failure has been observed, corresponding to the progressive peeling of the superimposed part of the ligaments. The load carrying capability of the cell remained close to the maximum load level until a displacement of 30 mm, as it is confirmed in Fig 10-b.

Figure 11 shows the course of the strain recorded by the gages SG2, SG4 and SG6 in TEST #1. The behavior of the SG1, SG3 and SG5 signals, acquired in symmetrical position with respect to the reported ones have been absolutely similar.
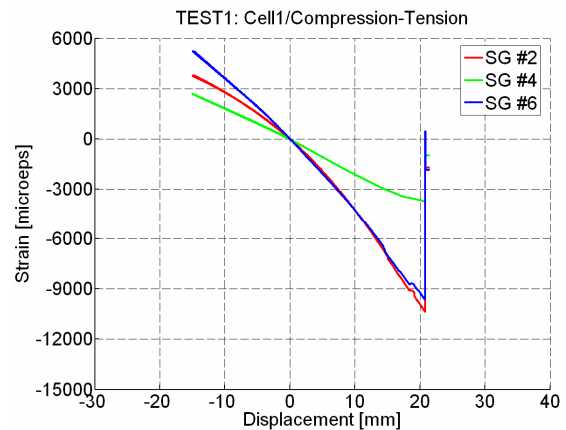

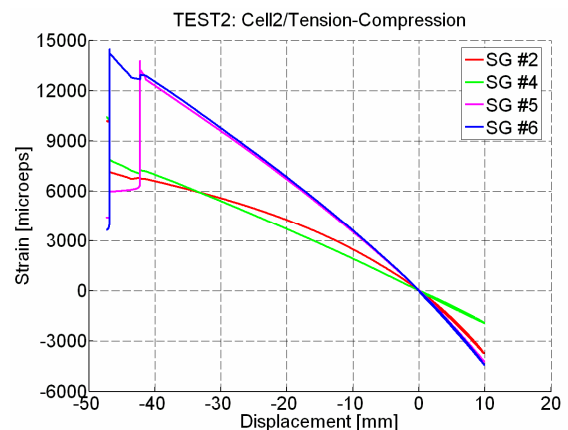Fig. 11. TEST #1: Strain vs displacement responses

Fig. 12. TEST #2: Strain vs displacement responses

It can be observed that, in tension, the strain levels SG2 and SG6, on the compressed side of the two ligaments converging on the constrained cylinders are similar and are about

three times the strain recorded near the central cylinder. As confirmed by the deformation shown in Fig. 9-c, the ligaments connected to the constrained cylinders are significantly bended. If a maximum admissible strain in compression of 0.01 is considered, the strain signals indicate that the compressive failure of the ligament would be achieved with a further small increment of the imposed displacement. Hence, although the presented results indicate that bonding is the actual weak point of the manufactured structure in tension, the bonding strength appears adequate to exploit almost the whole in-plane compressive strength of the composite ligaments. As far the compressive failure is concerned, the force vs. displacement curve referred to TEST #2 indicates that failure has been obtained at a displacement of almost -50 mm, corresponding to about 30% of the cell dimension. Figure 13 reports a sequence taken from TEST #2 showing the overall level of contraction of the cell obtained in the experiment. Failure has been obtained, in this case, for excessive bending of the ligaments in the two points evidenced in Fig. 13-b.
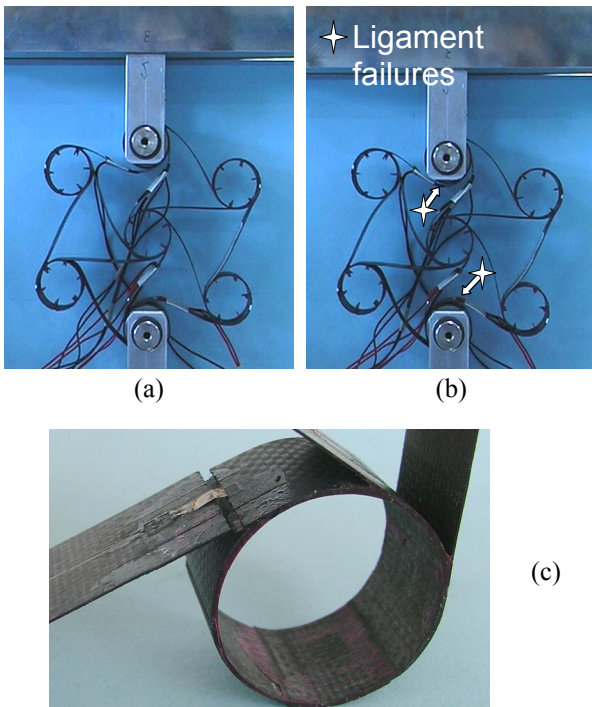

(a)   (b)

(c)

Fig. 13. TEST #2: deformation at 35 mm of displacement (a), at failure (b) and compressive failure mode (c)

Figure 13-c shows one of the constrained cylinder of the cell, after the removal from the test fixture. The breakage of the ligament is evident as well as the absence of visible damage in the bonding between the ligaments.

Figure 12 is referred to the strains signals recorded in test 2 by SG2, SG4, SG5 and SG6. It can be observed that the gages SG5 and SG6, located on the tensed side of the failed ligaments actually experienced the highest strain levels among the recorded ones. The failure of the ligaments occurred in correspondence of strain levels between 13000 and 14000 με. Compression appears less critical than tension as far as the cell strength is concerned. The visual inspection of the cell did not allow to evidence any damage in the adhesive film, so that the weak point of the structure can be considered, for this particular configuration, the bending strength of composite ligaments.

5 Modelling technique for strength prediction

5.1 Applied numerical approach

The possibility to numerically evaluate the non-linear response as well as the strength levels of the presented chiral structures could play a key role in the development of structures hosting composite chiral cores. The following paragraphs describe the application to the analyses of the performed experiments of a numerical approach devised to model stable and unstable delamination propagation in composite laminates.

The numerical prediction of the previously described experimental responses relies on the possibility to model the geometrical non-linearities exhibited by the cells, the failure due to the in-plane stress states experienced by the composite ligaments and the onset and propagation of damage in the adhesive layers between the ligaments. A possible strategy to fulfill such requirements is based on the numerical tools and approaches developed in [6-8] to model non-linear responses and failures of composites structures by means of explicit FE computation performed with the Simulia/Abaqus Explicit code. The biphasic material model described in [8] can be attributed at the plies included in a laminate shell element.

The constitutive response is capable to approximately represent matrix as well as fibre inelastic mechanisms by means of separated damage variables. A modelling technique to include interlaminar layers in FE schemes developed using shell elements is presented in [6,7]. The technique is based on the adoption of solid elements with a reduced integration scheme to connect shells representing composite sublaminates, as shown in Fig. 14-a. Such elements can transmit only out-of plane stress components, namely σ_{33}, σ_{13}, σ_{23} in material axis. Their constitutive response is characterized by a interface constitutive law with a bi-linear response capable to represent the strength as well as the toughness of the interlaminar layers. It has been verified that adoption of such technique does not modify the bending response of the assembled laminate [6,7].

5.2 Chiral cell model

To model the performed experiments on the chiral cells with Abaqus, the ligaments have been schematized by means of linear shell with a reduced integration scheme (S4R) having a non-linear response provided by the material model described in [8]. The adhesive layers between the ligaments have been represented by means of solid elements having the response based on the interface constitutive law presented in [6,7]. The obtained model of the cell is shown in Fig. 14-b. Two rigid cylinders have been included in the model and set in contact with the inner surface of the cell cylinders. Figure 14-c shows a detail of the central cylinder mesh evidencing the solid element representing the adhesive (dark elements) that connect the shells of the ligaments (light element).

The non-linear bi-phasic material law that models the plies in the laminate shell elements has been calibrated according to the stiffness properties given in Table 1. A brittle fibre failure has been set at $\varepsilon_{11} = \varepsilon_{22} = 0.013$ in tension and at $\varepsilon_{11} = \varepsilon_{22} = -0.095$ in compression, according to the results of previous characterization tests. Plies have been oriented so that the 2nd material direction is parallel to the ligament axes.

The toughness of the AFK-163-2K adhesive layer has been measured by means of ENF and DCB standard test performed on specimens made of two thick fabric sublaminates joined by a layer of pre-cracked adhesive film. Such tests allowed to evaluate the critical energy release rate for fracture evolving in mode I, $G_I = 0.519$ kJ/m^2, and in mode II, $G_{II} = 0.924$ kJ/m^2.

The peeling and the shear strength of the adhesive have been set to 20 MPa and 50 MPa, respectively. Tension and compression quasi-static explicit analyses have been carried out by imposing a gradually increasing velocity to the moveable cylinders.
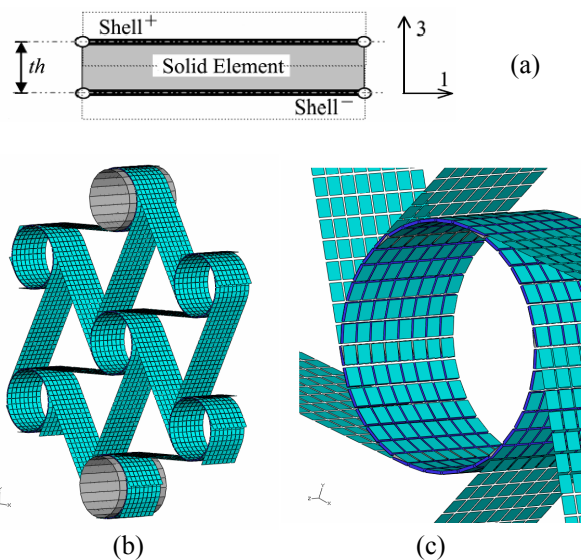

Fig. 14. Modelling technique for interlaminar (a) layers and developed model (b, c)

5.3 Numerical results

Figure 15 shows a sequence taken from the analyses of the compression test. It can be observed that he deformed shape are in good agreement with the experimental ones, shown in Fig. 9. The numerical model also identifies the zones where the maximum strains in the direction parallel to the ligament axis develop. The adopted material model for the plies predict the occurrence of a fibre failure close to the lower cylinder due to excessive compressive strain. Figure 15-d presents the contour of the fibre damage at 32 mm of deflection on the lower cylinder. As no contact has been set between the ligaments, the broken ligament

interpenetrates the cylinder, as also visible in Fig. 15-c. Failure mode is in qualitative agreement with the experimental evidence.
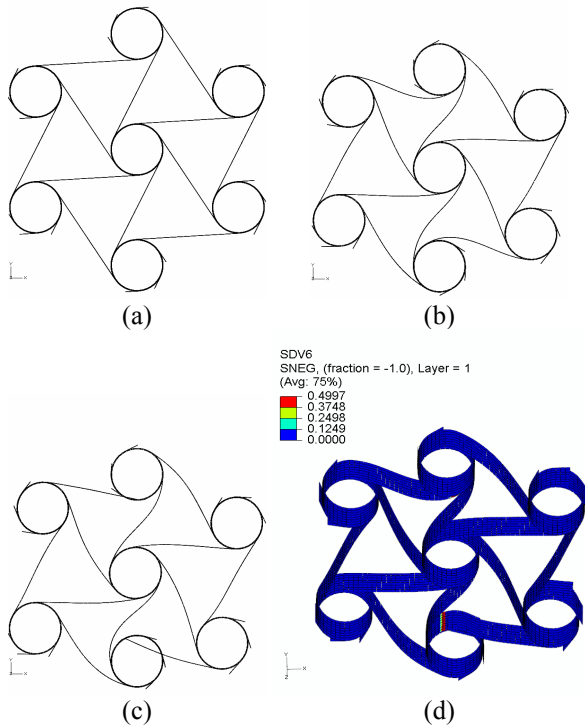

(a) (b)

(c) (d)

Fig. 15. Numerical deformation in the analysis of the compression test at 0 mm (a) 24 mm (b) 32 mm (c) of deflection and fibre damage at 32 mm of deflection (d)
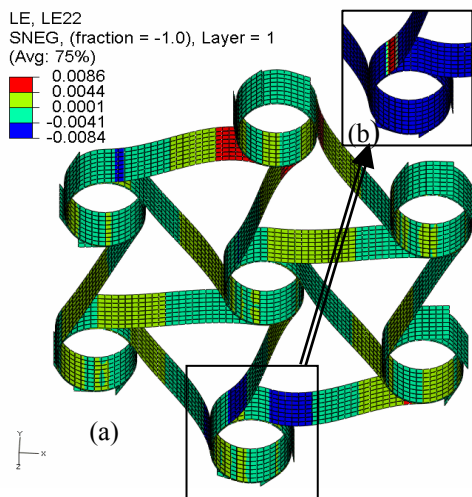

Fig 16 Contour of strain ε_{22} in the numerical analyses of tension test at 17 mm of deflection (a) and detail of the contour of fibre damage at 20 mm of deflection (b)

As far as the analyses of the tension test is concerned Fig. 16-a presents the contour of the ε_{22} strain at the top of the shells at 18 mm of deflection. The compressive strain on the vertical ligament close to the lower cylinder is

ε_{22} = -0.084. Such value is in good agreement with the strain recorded by SG2, reported in Fig. 11 but it is also quite close to the limit set in the model for the compressive failure of fibers. As a consequence, the numerical failure of the ligament occurs at 19 mm of deflection, as indicated in Fig. 16-b.

Figure 17 presents the correlation between the numerical and the experimental force vs. displacement curve and shows that the peculiar non-linear response of the cell is correctly predicted by the numerical analyses. Numerical failure is anticipated with respect to the experimental evidence. For compression this is probably due to an underestimation of the limit compressive strain in bending condition. The numerical curve in tension is slightly more compliant than the experimental ones and, moreover, the failure mode is not correctly reproduced, as ligament failure occurs before debonding.
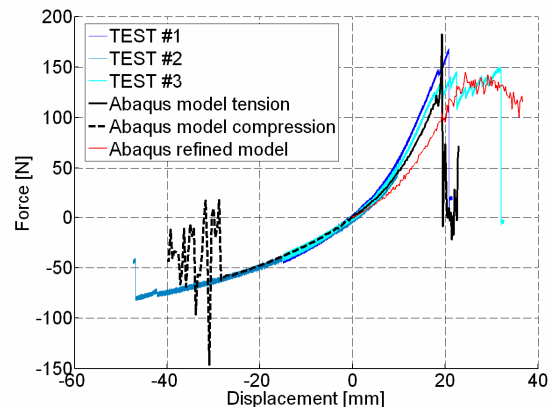

Fig 17 Numerical-experimental correlation

A more refined model of the chiral cell has been developed and the compressive limit strain has been raised to 0.011. Figure 18-a shows a detail of the upper cylinder in the new model. The refined mesh allows to better model the stress gradient in the solid elements representing the adhesive and this contributes to the onset of damage in solid elements. As a consequence of the introduced modification, the development and the progressive propagation of adhesive damage are modeled beyond 19 mm of tensile deflection, as shown in the sequence presented in Figg. 18-b and 18-d. As shown in Fig. 17, the mesh refinement increased the compliance of the model, that now underestimates the tensile

stiffness, but the force vs. displacement curve exhibits a post-failure progressive behavior that qualitatively matches the one recorded in TEST #3. The correct representation of the thickness and of the extension of the adhesive film as well as bending test performed on single ligaments are required to improve the stiffness correlation.
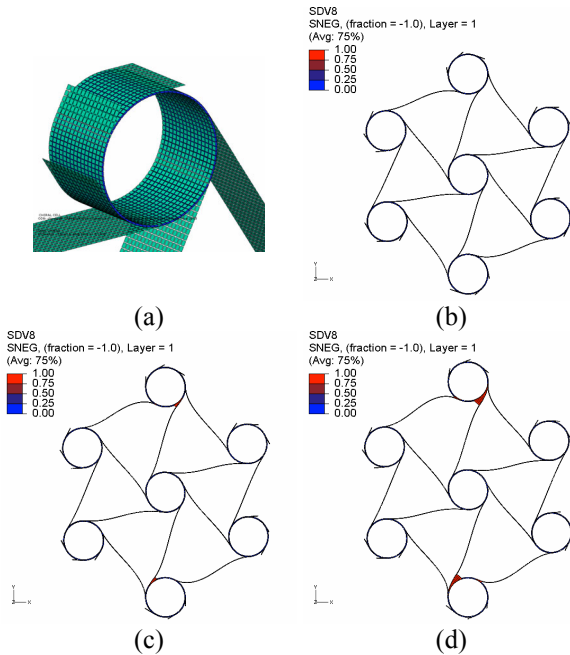

Fig. 18. Detail of the the refined model (a) and contour of interlaminar damage in the adhesive at 20 mm (b), 29 mm (c) and 36 mm of tensile deflection (d)

6 Conclusion

The presented numerical and experimental activities show that long fiber reinforced composites can be considered suitable candidate to exploit the morphing capability of chiral topologies.

The developed process allows to manufacture chiral cells that seems capable to work within a range between -9% ÷ +6% of the cell dimension without the activation of any inelastic behavior. Fatigue test are required to evaluate the true safe working interval for the cell included in a real-world structure.

The presented numerical approaches can be considered valuable tools to optimize the performance of chiral cores hosted in aircraft structures as well as to predict their strength. As far as these aspects are concerned, the experimental results indicates that non-linear geometrical effects can not be neglected in modeling the response of chiral structures.

References

[1] Bowman J, Sanders B and Weisshaar T. Identification of military morphing aircraft missions and morphing technology assessment. Proceedings of *SPIE Smart Materials and Structures*, San Diego, CA, 17 March, 2002, pp. 121-132.

[2] Monner H P, Sachau D and Breitbach E. Design Aspects of the Elastic Trailing Edge for an Adaptive Wing, *Research and Technology Agency*, Ottawa, Canada, October 18-21, pages 14/1 - 14/8, 1999.

[3] Buter A, Ehlert U C, Sachau D, and Breitbach E. Adaptive rotor blade concepts, direct twist and camber variation. Procedings of *AVT Symposium*, Braunschweig, 2000.

[4] Spadoni A and Ruzzene M. Numerical and Experimental Analysis of The Static Compliance of Chiral Truss-Core Airfoils. *Journal of Mechanics of Materials and Structures*, Vol. 2(5) pp. 965, 2007.

[5] Spadoni A and Ruzzene M. Static Aeroelastic Response of Chiral Truss-core Airfoils. *Journal of Intelligent Material Systems and Structures*, 5 2007.

[6] Airoldi A, Sala G and Bettini P. Evaluation of numerical approaches for the development of interlaminar damage in composite laminates. Proceedings of *16th International Conference on Composite Materials*, Kyoto, JN, July 2007.

[7] Airoldi A, Sala G and Pasqualini F. Experimental and numerical investigation on the failure modes of thick composite laminates. Proceedings of *25th International Congress of the Aeronautical Sciences*, Hamburg, Germany, 3-8 September 2006.

[8] Airoldi A, Lanzi L and Sala G. Shear Post-Buckling Behaviour of Glare Modeling Fiberglass Damage. *47th AIAA/ASME/ASCE/AHS/ASC Structures, Structural Dynamics and Material Conference and Exhibit*, Newport, Rhode Island, USA, 1-4 May, 2006, AIAA Paper 2006-2027, p. 1-17.